Journal of Electrostatics 123 (2023) 103815

Contents lists available at ScienceDirect

Journal of Electrostatics

journal homepage: www.elsevier.com/locate/elstat

Scaling relations for the geometry of wire-to-airfoil atmospheric ionic thrusters

Omar Kahol *, Marco Belan, Mattia Pacchiani, Domenico Montenero

Politecnico di Milano, Dipartimento di Scienze e Tecnologie Aerospaziali, 20156 Milano, Italy

ARTICLE INFO

Keywords:
EHD propulsion
Atmospheric ion thruster
Corona discharge

ABSTRACT

This work presents a multiparameter experimental investigation on the effects of geometrical parameters on the performance of corona thrusters. A scaling model is presented in order to define physically consistent reference values and dimensionless coefficients that describe the main performance indicators. Airfoil collectors of different thickness and chord are tested in a parallel array configuration at different spacings, gaps and voltages. Direct thrust and electrical measurements are performed and used to determine the dimensionless coefficients. The results identify scaling relations and indicate that collectors with short chord and adequate thickness maximize, within the investigated parameter space, the performance parameters.

1. Introduction

Since the beginning of the aviation era, aeroplanes have always been powered by moving parts propulsive systems such as propellers and turbine engines with consequent high consumption of fossil fuels. The new trend of scientific and technological development is oriented towards the reduction of carbon emissions in favor of renewable energies. In the aerospace sector, electrical propulsion techniques are regarded as a promising and valid alternative to fossil fuel ones [1,2]. Among all, ionic thrusters have been already widely and successfully used for space applications [3–5]. Although nowadays they are still not employed in atmospheric flight applications, in the last years the interest for Electrohydrodynamic (EHD) propulsion in this field is rapidly growing as an alternative to conventional engines. Ionic propulsion would provide several advantages for atmospheric flight such as the high efficiency in terms of thrust-to-power ratio, absence of moving parts, low maintenance, low noise emissions and the high sustainability of this kind of propulsive system deriving from electric power consumption [6–12].

An EHD thruster, in its simplest version, is composed by two electrodes separated by a distance called gap. The ion emitter is typically a metallic wire of radius smaller than 100 μm, while the ion collector is a larger electrode with a conductive surface that can assume different shapes. These simple devices exploit the corona effect to create an ionic wind able to generate a net thrust. A strong asymmetric electric field between the electrodes is imposed applying a sufficiently high voltage difference with a suitable power supply. The electric field ionizes the gas surrounding the emitter, in turn creating a corona discharge where the drifting motion of the ions transfers momentum to the neutral molecules.

Starting from these basic elements, there was an evolution along the years that has led to different configurations. The scientific progress has advanced from simple geometries with cylindrical collectors to more sophisticated ones with airfoil collectors, with the objective of optimizing the performance.

As depicted in Fig. 1, in each unit the emitter and the collector are separated by a gap d. The main geometric parameters for the collector are the chord c and the thickness t. This configuration can be replicated along the y direction, with spacing S, to obtain a multiple units configuration. The space between adjacent units is also indicated as *thruster cell*.

The aforementioned thruster configuration has already been studied and used in literature. As far as the applications are concerned, it was proved that the wire-to-airfoil configuration can successfully power a small airplane in sustained flight with power supply on board [13]. Moreover, a similar wire-to-airfoil configuration was used to build a lifter with outboard power supply, proving that optimized EHD configurations can produce a lifting force greater than the weight of the system [14,15].

More generally, the wire-to-airfoil configuration is object of studies exploring its capabilities by numerical simulations and experiments. Among them, drop airfoil were considered as suitable collector shapes in some works [16,17] and used in the mentioned ionocraft [15]. Symmetric NACA airfoils were considered in parametric studies [18–

* Corresponding author.
E-mail address: omar.kahol@mail.polimi.it (O. Kahol).

https://doi.org/10.1016/j.elstat.2023.103815
Received 9 December 2022; Received in revised form 15 March 2023; Accepted 3 May 2023
Available online 17 May 2023

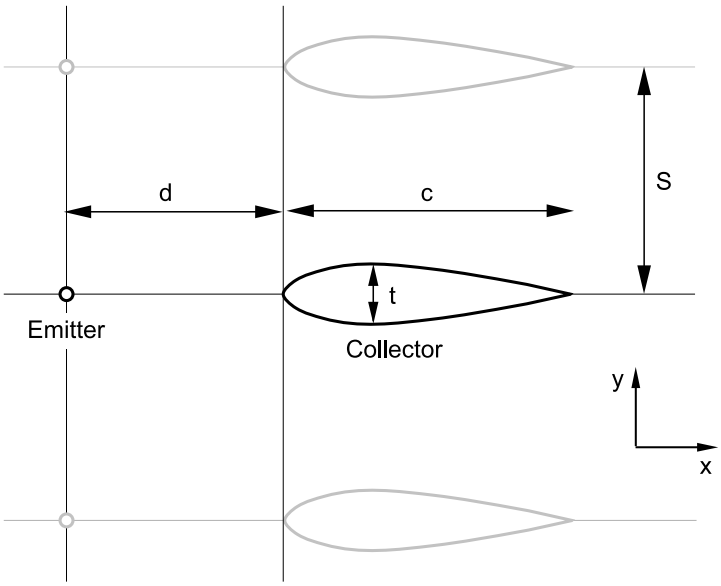

Fig. 1. Geometry and parameters of an EHD thruster in a multiple units wire-to-airfoil configuration.

20] revealing that optimal geometries can be identified within suitable parameter spaces; these airfoils were also used in the mentioned airplane [13].

A parameter of great importance is the gap between electrodes, in fact its influence on the performance parameters has been studied by several authors [10,15,21,22] discovering that a gap increase is beneficial for the thrust-to-power ratio but detrimental for the thrust density. It is also worth noting the use of airfoils as propeller blades with ionizing pins [9,12,23], however in this case the blades play the role of emitters.

Another noteworthy parameter is the wire diameter. In particular, emitters with a larger radius of curvature have been shown to have a negative impact on the overall performance of the thruster both in laboratory studies [15,22] and in numerical simulations [24–27].

This work intends to further explore the areas for improvement of thrusters performance by acting on the geometry and, in particular, on the airfoil shape. The thickness and the chord are identified as the two main variables. Using those parameters a symmetric 4 digit NACA airfoil can be generated. The underlying principle is linking chord and thickness to EHD thrust and aerodynamic drag, maximizing the performance. To complete the analysis, the effect of spacing and gap variations is also studied.

Given the large number of parameters involved, the work is supported by a dimensional analysis on the drift region equations that leads to define suitable dimensionless coefficients. This is done in order to properly describe the involved phenomena, by scaling the measured quantities with respect to physically meaningful reference values, and gives the chance to identify useful scaling relations.

The article is organized as follows: in Section 2 the dimensionless scaling model is developed; Section 3 presents the experimental setup used in this work and described in details the parameter space explored in the experimental investigation. Section 4 presents the results obtained within the experimental campaign and in Section 5 the conclusion are drawn.

2. Scaling

2.1. Physics and modeling

In the considered EHD applications, two distinct regions are present: the *ionization region* and the *drift region*. The ionization region near the emitter is dominated by the presence of a strong electric field which activates a plethora of ionization mechanisms that are capable of ionizing the gas. Beyond a certain distance, the electric field strength is no longer sufficient to sustain ionization and the ions enter the drift region, where their collisions with neutral molecules only result in a transfer of kinetic energy. Here the newly formed ions travel towards the collector under the influence of the electric field.

2.1.1. Ionization region

The earliest model of the ionization region is due to Peek [28] and Kapztov [29]: it sets a value for the *inception field*, E_i, that can be used to prescribe a boundary condition for the electric field. The main effect captured by Peek's law is the presence of an inception voltage, which corresponds to the voltage below which no current or thrust is measurable. This value significantly influences the current (and therefore the thrust) in the nominal corona regime, as it was initially noted by Townsend [30].

It is therefore possible to define a new dimensionless variable $\hat{V}$, called the *scaled voltage*, as the ratio between the applied voltage V_a and the inception voltage V_i:

$$\hat{V} = \frac{V_a}{V_i} \,. \tag{1}$$

The dependence of the EAD performance parameters, like thrust and power, on the scaled voltage is studied in detail in Appendix, which develops a 1D dimensionless analytical formulation.

This model assumes that changes in the ionization region, which may be caused by changes in the geometry, directly affect the value of the inception voltage. Correspondingly, also the scaled voltage will be affected.

2.1.2. Drift region

The physics of the drift region is well understood and, under suitable assumptions [31], can be described by the drift region equations

$$\begin{cases} \nabla \cdot \mathbf{E} = \rho_q / \epsilon_0 \\ \nabla \cdot \rho_q \left(\mu_q \mathbf{E} + \mathbf{u} \right) = 0 \\ \rho \mathbf{u} \cdot \nabla \mathbf{u} = -\nabla P + \mu \nabla^2 \mathbf{u} + \rho_q \mathbf{E} \end{cases} \tag{2}$$

where $\mathbf{E}$ is the electric field, ρ_q is the charge density, μ_q the ion mobility and $\mathbf{u}, \rho, P$ the velocity, density and pressure of the gas, respectively. The first equation is Maxwell's law of electric fields while the second one is the steady state conservation equation for the charges motion without diffusion. The third equation is the conservation of momentum for the neutral gas. The latter contains the term $\rho_q \mathbf{E}$ that represents the momentum transfer due to collisions with ions.

2.2. Scaling of the drift region

The main physical parameters chosen to start building dimensionless quantities are

1. Applied voltage, V_a.
2. Gap, d.

The nondimensionalization of the equations is carried out starting with the following relations:

1. $\mathbf{x} = d\ \hat{\mathbf{x}}$, the reference system is made dimensionless by the gap d.
2. $\mathbf{E} = (V_a/d)\ \hat{\mathbf{E}}$, The electric field is scaled by the ratio of the applied voltage and the gap.
3. $\rho_q = \rho_0\ \hat{\rho_q}$, the space charge density is scaled by a reference value.
4. $\mathbf{u} = u_0\ \hat{\mathbf{u}}$, the hydrodynamic velocity is scaled by a reference value.
5. $P = P_0\ \hat{P}$, the pressure is scaled by a reference value.

The reference values ρ_0, u_0, P_0 are progressively exposed in what follows. The introduction of the aforementioned scaling in Eqs. (2) yields

$$\begin{cases} \hat{\nabla}\cdot\hat{\mathbf{E}} = \dfrac{\rho_0}{\epsilon_0\dfrac{V_a}{d^2}}\hat{\rho_q} \\ \hat{\nabla}\cdot\hat{\rho_q}\left(\hat{\mathbf{E}} + \dfrac{u_0}{\mu_q\dfrac{V_a}{d}}\hat{\mathbf{u}}\right) = 0 \\ \hat{\mathbf{u}}\cdot\hat{\nabla}\hat{\mathbf{u}} = -\dfrac{P_0}{\rho u_0^2}\hat{\nabla}\hat{P} + \dfrac{\rho_0 V_a}{\rho u_0^2}\hat{\rho}_q\hat{\mathbf{E}} + \dfrac{\nu}{u_0 d}\hat{\nabla}^2\hat{\mathbf{u}} \end{cases} \tag{3}$$

Eqs. (3) represent the dimensionless version of the drift region equations, provided that ρ_0, u_0, P_0 are properly defined. As for the charge density, a reference value can be defined in such a way that the multiplicative term in the first equation has order 1:

$$\rho_0 = \epsilon_0\frac{V_a}{d^2}\,. \tag{4}$$

As it will be shown later, this assumption leads to retrieve the Mott-Gurney law for the current density [32], which is a proper model for the current density in a 1D geometry.

Under the hypothesis of no external convection, only collisions between ions and neutral gas molecules are responsible for the creation of a mean flow. This suggests that the order of magnitude of the kinetic energy of the flow ρu_0^2 is comparable to the ion potential energy $\rho_0 V_a$, and leads to set

$$u_0 = \sqrt{\frac{\rho_0}{\rho}V_a} = \frac{V_a}{d}\sqrt{\frac{\epsilon_0}{\rho}}\,, \tag{5}$$

where Eq. (4) was used. The pressure reference term is similarly defined using the kinetic energy term because ionic thrusters in still air create a suction force that results in a negative pressure gradient at the inlet section, thus it is convenient to set

$$P_0 = \rho u_0^2 = \epsilon_0\frac{V_a^2}{d^2}. \tag{6}$$

Using the aforementioned assumptions the dimensionless equations become

$$\begin{cases} \hat{\nabla}\cdot\hat{\mathbf{E}} = \hat{\rho_q} \\ \hat{\nabla}\cdot\hat{\rho_q}\left(\hat{\mathbf{E}} + R_v\hat{\mathbf{u}}\right) = 0 \\ \hat{\mathbf{u}}\cdot\hat{\nabla}\hat{\mathbf{u}} = -\hat{\nabla}\hat{P} + \hat{\rho}_q\hat{\mathbf{E}} + \dfrac{1}{Re_d}\hat{\nabla}^2\hat{\mathbf{u}}\,, \end{cases} \tag{7}$$

where two new dimensionless numbers appear:

$$Re_d = \frac{u_0 d}{\nu} = \frac{V_a}{\nu}\sqrt{\frac{\epsilon_0}{\rho}}\,, \tag{8}$$

$$R_v = \frac{u_0}{u_i} = \frac{1}{\mu_q}\sqrt{\frac{\epsilon_0}{\rho}}. \tag{9}$$

Re_d is a Reynolds number based on the gap, appearing in the momentum equation. It is generally related to the size of the thruster through the gap, and in the present experiment ranges from 1000 to 4000 depending on the applied voltage value.

R_v, appearing in the ion transport equation, is the ratio between the reference convective velocity u_0 and the reference ion drift velocity $u_i = \mu_q V_a/d$. For a thruster in still air, $R_v \sim 10^{-2}$ and is typically negligible.

According to the previously defined reference values, the current density can be made dimensionless in the following form:

$$\mathbf{j} = \rho_q\left(\mu_q\mathbf{E} + \mathbf{u}\right) = \epsilon_0\mu_q\frac{V_a^2}{d^3}\hat{\mathbf{j}}\,, \tag{10}$$

where the dimensionless quantity is

$$\hat{\mathbf{j}} = \hat{\rho_q}\left(\hat{\mathbf{E}} + \frac{1}{\mu_q}\sqrt{\frac{\epsilon_0}{\rho}}\hat{\mathbf{u}}\right). \tag{11}$$

In Appendix it will be shown that in 1D, under suitable assumptions, the dimensionless current density becomes $\hat{\jmath} = 9/8$, which in Eq. (10) yields the dimensional functional form of the current density predicted by the Mott-Gurney law [32].

2.3. Integral quantities

Using the reference values defined above for the local quantities, it is possible to compute reference values for the integral quantities.

2.3.1. Thrust

The thrust force generated is defined as the integral of the EHD force density. In a 2D framework as in Fig. 1, the derived value is a thrust per unit span, where the span b extends along the z direction, normal to the xy plane defined in figure:

$$\frac{T}{b} = \int_\Omega \rho_q E_x\ \mathrm{d}\Omega \tag{12}$$

where E_x is the x component of $\mathbf{E}$ and Ω is the 2D section in the xy plane of a volume extending along the z direction with constant cross section. Using the chosen reference values, the thrust integral becomes

$$\frac{T}{b} = \epsilon_0\frac{V_a^2}{d}\int_{\hat{\Omega}}\hat{\rho}_q\hat{E}_x\ \mathrm{d}\hat{\Omega} = \epsilon_0\frac{V_a^2}{d}C_T \tag{13}$$

and the thrust coefficient C_T turns out as a dimensionless thrust integral. Besides thrust, another force must be considered: the aerodynamic drag D on the electrodes (negligible for the emitters in the present study). The difference between thrust and drag may be called *effective thrust*:

$$T_e = T - D. \tag{14}$$

Using the aerodynamic scaling laws, it is possible to express this quantity through a dimensionless coefficient:

$$\frac{T_e}{b} = \epsilon_0\frac{V_a^2}{d}C_T - \frac{1}{2}\rho u_0^2\ c\ C_D = \epsilon_0\frac{V_a^2}{d}\left(C_T - \frac{1}{2}\frac{c}{d}C_D\right) = \epsilon_0\frac{V_a^2}{d}\ C_{Te}\,. \tag{15}$$

The *effective thrust coefficient* $C_{Te} = C_T - \frac{1}{2}(c/d)C_D$ inherently accounts also for the aerodynamic drag. It is interesting to observe that the efficiency, defined as the ratio between the electrical thrust and the drag [20], increases as the ratio c/d decreases, i.e. it increases by shortening the airfoil chord with a given gap:

$$\theta = \frac{T}{D} = 2\ \frac{d}{c}\ \frac{C_T}{C_D}. \tag{16}$$

2.4. Electrical power

The power consumption per unit span can be computed using the integral

$$\frac{P}{b} = \int_{\Omega} \mathbf{j} \cdot \mathbf{E} \, \mathrm{d}\Omega. \tag{17}$$

The application of the presented scaling yields

$$\frac{P}{b} = \mu_q \epsilon_0 \frac{V_a^3}{d^2} \int_{\hat{\Omega}} \hat{\mathbf{j}} \cdot \hat{\mathbf{E}} \, \mathrm{d}\hat{\Omega} \; = \; \mu_q \epsilon_0 \frac{V_a^3}{d^2} \, C_P \tag{18}$$

where C_P is the power coefficient.

2.4.1. Mechanical power

The mechanical power transferred to the gas is the volume integral of the mechanical power of the EHD force

$$\frac{P_u}{b} = \int_{\Omega} \mathbf{u} \cdot \rho_q \mathbf{E} \, \mathrm{d}\Omega. \tag{19}$$

The latter is scaled as

$$\frac{P_u}{b} = \epsilon_0 \frac{V_a^3}{d^2} \sqrt{\frac{\epsilon_0}{\rho}} \int_{\hat{\Omega}} \hat{\rho}_q \hat{\mathbf{u}} \cdot \hat{\mathbf{E}} \, \mathrm{d}\hat{\Omega} \; = \; \epsilon_0 \frac{V_a^3}{d^2} \sqrt{\frac{\epsilon_0}{\rho}} \, C_{Pu} \tag{20}$$

where C_{Pu} is the mechanical power coefficient.

2.4.2. Performance parameters

Several performance parameters can be put in dimensionless form according to the previous scaling, always accounting for the drag effects.

The effective thrust to power ratio can be expressed as

$$\frac{T_e}{P} = \frac{\mu_q d}{V_a} \frac{C_{Te}}{C_P} = \frac{\mu_q d}{V_a} \, C_{TPe}. \tag{21}$$

A meaningful frontal area $A = S \, b$ can be defined, with reference to Fig. 1, as (frontal size × span) or (spacing × span) on the yz plane. In this way, an effective surface thrust density can be defined as

$$\frac{T_e}{A} = \epsilon_0 \frac{V_a^2}{Sd} C_{Te} = \epsilon_0 \frac{V_a^2}{d^2} \frac{d}{S} \, C_{Te} = \epsilon_0 \frac{V_a^2}{d^2} \, C_{TAe} \, , \tag{22}$$

having introduced the effective surface thrust density coefficient

$$C_{TAe} = \frac{d}{S} C_{Te} \, . \tag{23}$$

Once a suitable reference area has been defined, the extension to an effective volumetric thrust density is straightforward by considering a volume $A \, l$, where l is the thruster size (or a meaningful length) along the x direction:

$$\frac{T_e}{Al} = \epsilon_0 \frac{V_a^2}{Sld} C_{Te} = \epsilon_0 \frac{V_a^2}{d^3} \frac{d^2}{Sl} C_{Te} = \epsilon_0 \frac{V_a^2}{d^3} C_{TVe} \, , \tag{24}$$

having introduced the effective volumetric thrust density coefficient

$$C_{TVe} = \frac{d^2}{Sl} C_{Te} \tag{25}$$

Finally, the mechanical-to-electrical power ratio can be introduced as electro-mechanical efficiency, describing the fraction of electrical energy that is converted into mechanical energy:

$$\eta = \frac{P_u}{P} = \frac{1}{\mu_q} \sqrt{\frac{\epsilon_0}{\rho}} \frac{C_{Pu}}{C_P} \, , \tag{26}$$

and in dimensionless form becomes C_{Pu}/C_P.

All the scaled quantities are presented in the summary Tables 1 and 2.

Table 1
Integral quantities.

Name	Symbol	Reference value	Dimensionless coefficient
Effective thrust	$\frac{T_e}{b}$	$\epsilon_0 \frac{V_a^2}{d}$	C_{Te}
Electrical power	$\frac{P}{b}$	$\mu_q \epsilon_0 \frac{V_a^3}{d^2}$	C_P
Mechanical power	$\frac{P_u}{b}$	$\epsilon_0 \frac{V_a^3}{d^2} \sqrt{\frac{\epsilon_0}{\rho}}$	C_{Pu}

Table 2
Performance parameters.

Name	Symbol	Reference value	Dimensionless coefficient
Thrust to power ratio	$\frac{T_e}{P}$	$\frac{\mu_q d}{V_a}$	C_{TPe}
Surface thrust density	$\frac{T_e}{A}$	$\epsilon_0 \frac{V_a^2}{d^2}$	C_{TAe}
Volumetric thrust density	$\frac{T_e}{Al}$	$\epsilon_0 \frac{V_a^2}{d^3}$	C_{TVe}
Electro-mechanical efficiency	$\frac{P_u}{P}$	$\frac{1}{\mu_q} \sqrt{\frac{\epsilon_0}{\rho}}$	$\frac{C_{Pu}}{C_P}$

3. Experimental setup

A custom made experimental setup was employed in order to perform direct thrust and electric measurements.

The test rig, already used in a previous work [19], is depicted in Fig. 2 and its components present minor modifications in the support structures. The results are analyzed in a reference system consistent with Fig. 1, with axes referred to the collectors; thus the directions are x (chordwise), y (normal to the airfoils chords) and z (spanwise).

Rapid prototyping was extensively used to manufacture ad-hoc components, resulting in a good compromise between design flexibility and dimensional accuracy.

Fig. 3 gives a detailed view of the electrical components and connections, similar to the circuit used in [19]. A 0.996 MΩ ballast resistor R_b is connected in series with the thruster. A voltage divider with a total resistance $R_{p1} + R_{p2} = 152.9$ MΩ is used to read the voltage across the thruster. Shunt resistors of selectable resistance R_s are employed in order to perform direct current measurements.

The collector system is realized by means of 5 parallel airfoils with a span of 120 mm. The number of airfoils is chosen to create a good approximation of the periodic conditions that occur in an infinite array. The collectors are coated with aluminum and connected to ground. All the airfoil ends are protected by insulating caps to minimize the end effects on the electric field. The inter-collector spacing can be varied in a discrete fashion thanks to the support system.

The emitter system, connected to the positive pole of the power supply, is realized by means of a 30 μm constantan wire which is tensed above the collectors. The test rig allows for discrete variations of the gap and custom made pegs regulate the inter-emitter spacing. Suitable protections (not shown in figure for clarity) are employed to insulate the ends of the emitters and reduce electrical losses.

The size and the shape of the connecting wires are chosen so as to minimize their effect on the thrust measurements.

3.1. Thrust measurements

Three identical load cells are used for the load measurements, resulting in an appropriate trade-off between accuracy and full scale value. These are grounded and arranged in a radial configuration with equal angular spacing and mounted on a rigid plate. The full details of this system are described in [19].

To enhance the accuracy and precision of force transfer in the test rig, a new mounting system was developed and is illustrated in Fig. 4.

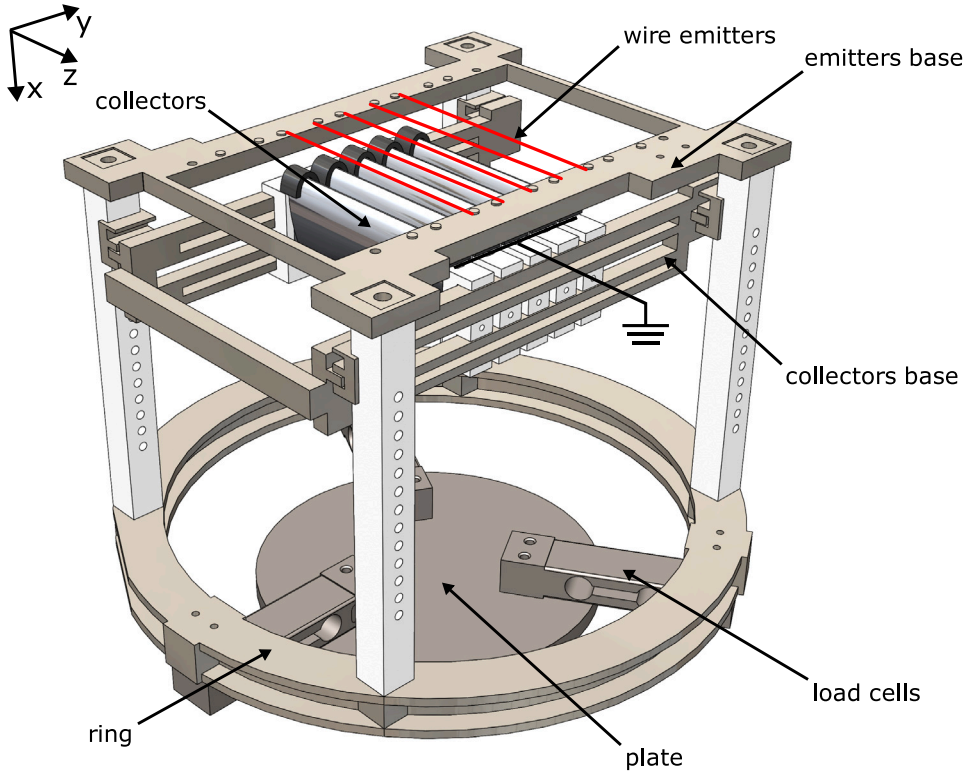

Fig. 2. Experimental setup.

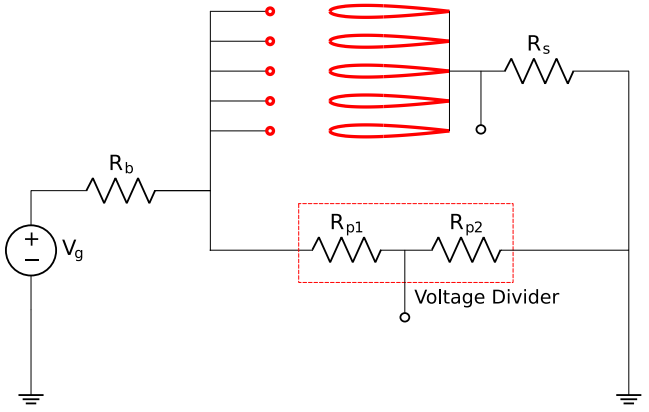

Fig. 3. Electric circuit.

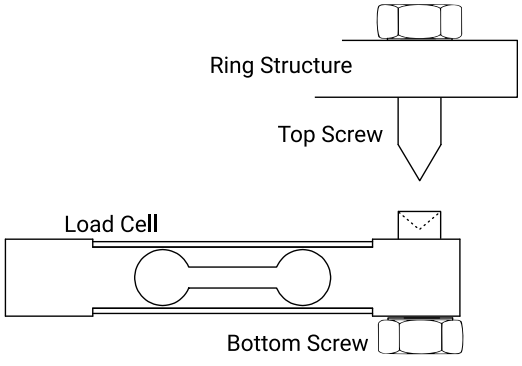

Fig. 4. Detail of the mounting mechanism (not to scale).

Each load cell is equipped with a screw featuring a 90° conical hole at the end. Three screws with cone-shaped ends that have a 60° angle are then threaded in a radial arrangement onto the ring structure. The structure is then placed on top of the load cells, so that each top screw make contact with the corresponding load cell screw through a minimal area. By ensuring that contact and force transmission occur at a single point for each cell, which is a fixed distance from the load cell mounting point, the lever arm is kept constant, leading to more consistent and accurate results.

The effective thrust is computed taking the difference $s_{\text{off}} - s_{\text{on}}$ between the load cells output signal when the thruster is switched off and on, and multiplying this value by the calibration constant of the system k_{cell}:

$$T_e = k_{\text{cell}} \left(s_{\text{off}} - s_{\text{on}} \right). \tag{27}$$

Multiple measurements are taken in order to ensure repeatability and perform uncertainty estimation. All measurements are referenced to a single cell and reported in dimensionless formulation by scaling with the reference value $T_{\text{ref}} = \epsilon_0 V_a^2 / d$ and the span b as described in Section 2:

$$C_{Te} = \frac{T_e}{5\, T_{\text{ref}}\, b}. \tag{28}$$

3.2. Electrical measurements

The electrical power consumption is measured during each thrust measurement process. It is computed from the voltage, read by the voltage divider with an accuracy of ± 30 V, and the current consumption, read by an ammeter with an accuracy of ±0.005 mA. Similarly to the thrust measurements, the power consumption is made dimensionless and referenced to a single unit:

$$C_P = \frac{P}{5\, P_{\text{ref}}\, b}. \tag{29}$$

The ignition voltage V_i is measured by inserting a 1.10 kΩ shunt resistor R_s as in Fig. 3 and assuming that a valid V_i value corresponds to

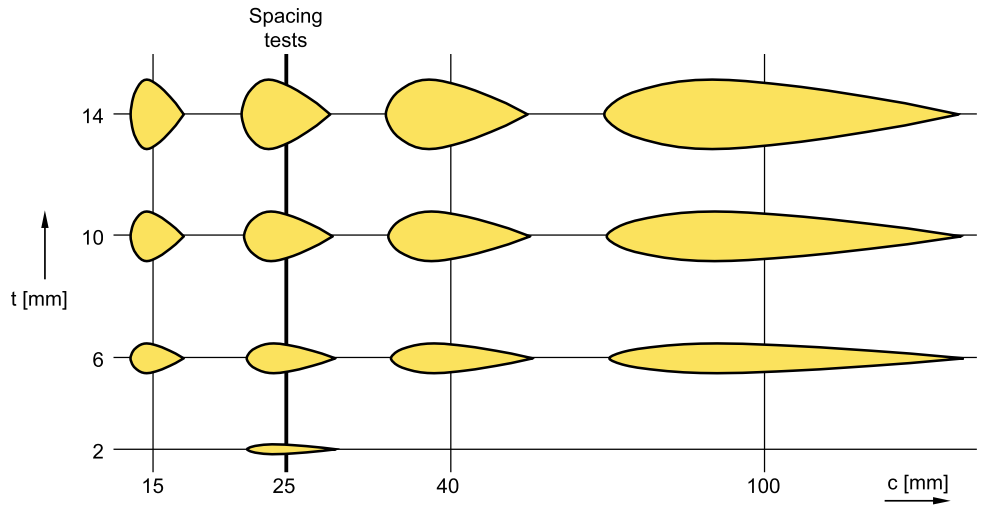

Fig. 5. Parameter space of airfoils collectors.

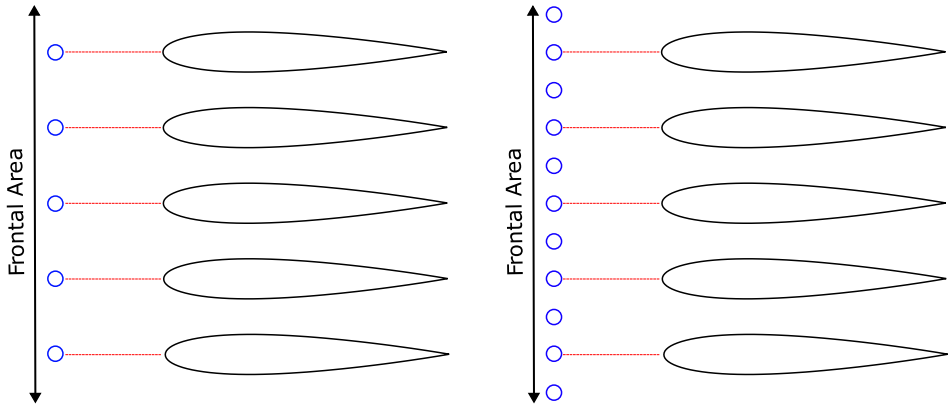

(a) Single Emitter (b) Double Emitter

Fig. 6. Periodic single and double emitter configurations.

a mean current greater than 3 times the rms noise signal (3σ criterion). This ensures an uncertainty in the order of 200 V.

3.3. Parameter space

The primary design variable in this work is the shape of the collectors, identifying the thickness and the chord as the main parameters which are used to generate a corresponding NACA 4-digit airfoil.

Fig. 5 shows the studied airfoil shapes. The investigated chords are 15, 25, 40 and 100 mm. Each chord family presents airfoils with variable thickness of 6, 10 and 14 mm. A further airfoil with chord 25 mm and thickness 2 mm was introduced during the tests to corroborate the experimental trends. Each configuration will be indicated using CxxTyySzz, where xx indicates the chord in mm, yy the thickness in mm and zz the spacing between units in mm.

The general criteria for defining this space are exposed in what follows: airfoils with very long chords are not efficient since they introduce a large amount of parasitic drag due to wall stress. Thus, there is no use in extending the space towards the right side since long airfoils are not an efficient solution for the design of an EHD thruster. Decreasing the chord while keeping the thickness constant would, on the one hand, keep a similar discharge section and consequently a similar electrical thrust; on the other hand, the t/c shape parameter would increase leading to bluff shapes and worsening the aerodynamic performance. Also an increase of thickness keeping the same chord leads to bluff bodies. Consequently, extensions towards the top and left of the parameter space are not viable either. This indicates that a local optimum could be found in the bottom zone of the parameter space, particularly on the left side. However, this region is bounded by some technical limits, since thin and short airfoils may create structural and manufacturing issues. First, these shapes have a lower stiffness compared to thicker airfoils and may introduce misalignments in the electric and motion fields. Secondly, manufacturing such electrodes may lead to several problems depending on the technology, such as the accuracy of 3D prototyping and milling or the preparation of composite structures (for the present work, the limiting factor is presumably the spatial accuracy of the 3D printer).

The dependence of the performance indicators on the gap d is of uttermost importance since the scaling introduced in Section 2 uses that dimension as a reference for all the other lengths. For this reason, specific tests are devoted to explore the dependence on the gap value. Other tests introduce the voltage variation, since the electric field scale is set by V_a and d. Further tests are introduced in order to study the dependence on the spacing S, a topic already considered on a smaller parameter space in [18].

Moreover, additional experiments are performed by exploring the differences between the single emitter (SE) and double emitter (DE) configuration shown in Fig. 6, since in a previous work [19] the double

emitter system was shown to have a beneficial effect both on the thrust density and on the thrust to power ratio in a periodic configuration.

The chances of varying c, t, d, V_a, S potentially give rise to an enormous number of combinations, for which it is necessary to establish an investigation criterion, keeping the laboratory time within reasonable limits. In what follows, the parameters are varied separately starting from a standard configuration based on previous investigations, namely:

$$\begin{aligned}&\text{gap } d = 20 \text{ mm; voltage } V_a = 20 \text{ kV;}\\ &\text{spacing } S = 35 \text{ mm; single emitter.}\end{aligned} \tag{30}$$

In particular, an initial evaluation is performed for all airfoils in Fig. 5 with this standard configuration. Then, a subspace with chord 25 mm (thick line in Fig. 5) is selected for further tests, including the spacing dependence in both single and double emitter configuration. Afterwards, the C25T6 airfoil is selected for a study of the gap and voltage dependence.

All tests were performed in a laboratory environment with a temperature of (20 ± 1) °C and a relative humidity range of 45% to 55%.

4. Results

4.1. Chord and thickness dependence

In this section, the effect of the chord and of the thickness on the performance of the thruster is presented. The evaluation is done in the standard conditions (30). Fig. 7 shows the behavior of the effective thrust, power and effective thrust to power coefficients for the different airfoils investigated as a function of the thickness.

The behavior of C_{Te}, shown in Fig. 7(a), is influenced by electrical and aerodynamic parameters. On one hand, increasing the thickness has a beneficial effect on the generated electrical thrust since the discharge section increases [18]. On the other hand, an increase in the thickness increases the t/c ratio which makes the airfoil less aerodynamic; moreover, it decreases the S/t parameter causing a worsening of the aerodynamic performance due to blockage effects [18]. The combination of these effects results in the presence of a local maximum as function of thickness for a given chord. Both the C100 and C40 families present this maximum in the corresponding T10 airfoil while the T14 airfoil suffers from blockage effects. The C25 family presents this maximum in the T6 airfoil since the C25T10 airfoil has a shape with poor aerodynamics. The local maximum for the C15 chord family should presumably appear on the left, outside the investigated parameter space.

Looking at Fig. 7(a) at constant thickness and variable chord it is possible to see that decreasing the chord with respect to well-known 100 mm case [13,18,19] is generally beneficial. This is because a reduction of the chord decreases the weight of the drag in the effective thrust coefficient $C_{Te} = C_T - \frac{1}{2}(c/d)C_D$, after Eq. (15). This is possible until the t/c parameter becomes too large, leading to a bluff airfoil which favors flow separation and the related drag increase.

Overall, the global maximum for C_{Te} in the parameter space is represented by the C25T6 airfoil. It remains unclear whether the C15T2 airfoil, not present in this parameter space because of manufacturing issues, could have a higher thrust. However, the investigated trends indicate that smaller and thinner airfoils could presumably increase the effective thrust in the order of 15%.

The power coefficient, being less influenced by aerodynamics, shows a simpler behavior. Similarly to the thrust coefficient, increasing the thickness produces an increase of the power coefficient because also the discharge section grows. Decreasing the chord also increases the power coefficient. This is probably due to the fact that a decrease in the chord has the effect of compressing the airfoil shape closer to the emitter, as shown in Fig. 8. This flattens the leading edge and moves the section with maximum thickness closer to the emitter, leading to an increase in current consumption.

As for thrust to power, C_{TPe} shows the combination of every effect mentioned so far. It is interesting to observe that, as the chord is decreased, there is a slight increase of C_{TPe} followed by a decrease. This indicates that a further extension of the parameter space by reducing chord and thickness, although beneficial for the total trust, would not necessarily improve C_{TPe}.

It is worth noting that in Fig. 7 the dimensionless coefficients trends correspond to the dimensional trends. In fact, as presented in Tables 1 and 2, each dimensional quantity can be written as the product of the relevant coefficient and reference factor, as for instance $T_e = C_{Te}T_{ref}$, and in the data above the reference factors are constant, given the experiment conditions. Instead, other results in the followings, as the ones about the gap effects, include also combined variations of coefficients and reference factors.

Fig. 9 shows the behavior of the Effective Volumetric Thrust Coefficient as function of the collector thickness. In Fig. 9(a) the reference volume is the one of a thruster unit $S\,(d + c)\,b$ and is an indicator of the spatial size of a single unit or cell; this indicator can be useful in studying the benefits of a multiple units configuration. In Fig. 9(b) the reference volume $(t\,c\,b)$ is proportional to the volume of a collector, and it is an indicator of the mass of the airfoil, if the collector is fully filled. Both these coefficients suggest that moving towards shorter and thinner collectors is beneficial.

The most important design parameters available for an optimization process are C_{TAe}, C_{TVe} and C_{TPe}. A local optimization must account for the weight assigned to each performance indicator and consider structural and manufacturing parameters. It is however clear that airfoils with large chords are inefficient and a reduction is suggested. In this work, the C25 family is identified as the global optimum since it results in an acceptable trade-off between the above parameters.

4.2. Spacing variation

The dependence on the spacing between units has already been studied by several authors [18,22,33]. In particular, a study on the C100 family [18] found that reducing the spacing between units results in a trade-off between the total thrust generated, which decreases by aerodynamic blockage as the spacing diminishes, and the surface thrust density, which presents a local maximum. Another work [33] showed that lowering the emitter spacing (i.e. increasing the emitter density) is not always beneficial because of the electrostatic interaction between close wires. This is known as *shielding*, as it limits the corona inception of closely packed wires.

Fig. 10 shows the behavior of the ignition voltage as function of the spacing between C25 airfoils under the standard conditions (30). The differences between airfoils of different thicknesses are not clearly measurable since they fall within experimental errors. It is however evident that decreasing the spacing favors the electrostatic interaction between the emitters, and this results in an increase of the ignition voltage.

Fig. 11 shows the behavior of all the performance parameters versus the spacing, for thrusters with one emitter per collector (SE configuration) as in the previously presented results. The plots of C_{Te} and C_P show the experimental data points as well as the relevant fits, already introduced in a previous work [18]:

$$\begin{cases}\dfrac{T}{b} = k_1\left(1 - k_2 e^{-k_3 s}\right)\\[2ex] \dfrac{P}{b} = k_4\left(1 - k_5 e^{-k_6 s}\right)\end{cases}. \tag{31}$$

The fits for C_{TAe} and C_{TPe} are derived from the previous ones. Fig. 11(a) shows that C_{Te} decreases as the spacing is reduced. This effect is believed to be a combination of both the aerodynamic blockage and the electrostatic shielding, progressively important as the spacing decreases. The power coefficient shows a similar behavior but the

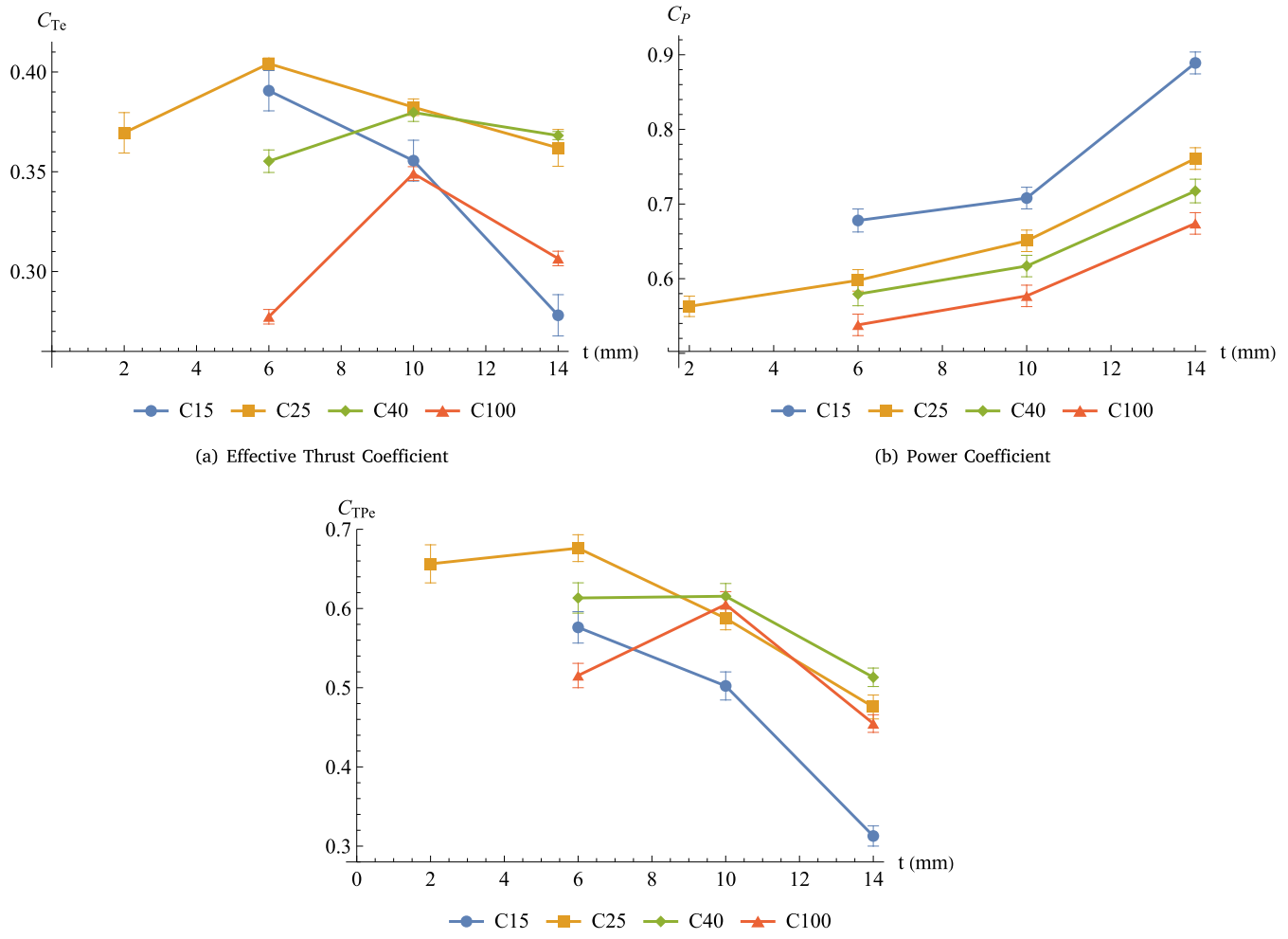

(a) Effective Thrust Coefficient

(b) Power Coefficient

(c) Effective Thrust to Power Coefficient

Fig. 7. Evaluation of the performance indicators, for each chord, as a function of the airfoil thickness.

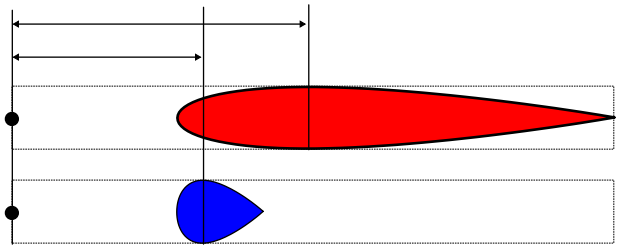

Fig. 8. Distance between emitter and maximum thickness section of the airfoil for two collectors of different chord and equal thickness.

exponential trend is less visible. This is because the power is less influenced by aerodynamics than by the electrostatic interaction, which is more important at small spacings.

C_{TAe} increases as the spacing is decreased but reaches a local maximum, then it drops following the effective thrust. The C25T2 airfoil reaches the highest effective thrust density C_{TAe} because aerodynamic losses become important only at very low spacings, given the fact that the airfoil (NACA0008) has a low t/c and hence a favorable slender shape.

Overall, Fig. 11(d) shows that a global maximum, in the considered space, is found for the C25T2 airfoil which maximizes the effective thrust density coefficient given a desired effective thrust to power and viceversa.

Fig. 12 shows the same analysis, repeated for the C25 family in a double emitter (DE) periodic configuration. In this case the spacing is S between collectors and $S/2$ between emitters, as in Fig. 6b. It is possible to see that at large spacings, a DE configuration boosts the generated thrust keeping the same power consumption, a behavior already evidenced in [19].

Again, it is possible to fit with an exponential behavior both the effective thrust and the power consumption. The effective thrust density admits a local maximum, reached by the C25T2 configuration, but the value is smaller than for the SE configuration. In fact, a DE configuration becomes unfavorable at low spacings because the double number of emitters may more easily cause the shielding phenomenon [33]. Accordingly, there is a performance drop for the C25T2 airfoil even if it is thin and aerodynamically capable of working at low spacing.

The curves in Fig. 12(d) show that C25T2 still exceeds C25T6 in the DE case, although the differences are small, and at large spacings the two airfoils have a similar C_{TPe}.

Further details about the C25T2 are presented in Fig. 13, which compares its SE and DE performance curves. It is seen that the DE configuration maximizes the thrust to power at high spacings while the SE configuration maximizes the surface thrust density at low spacings.

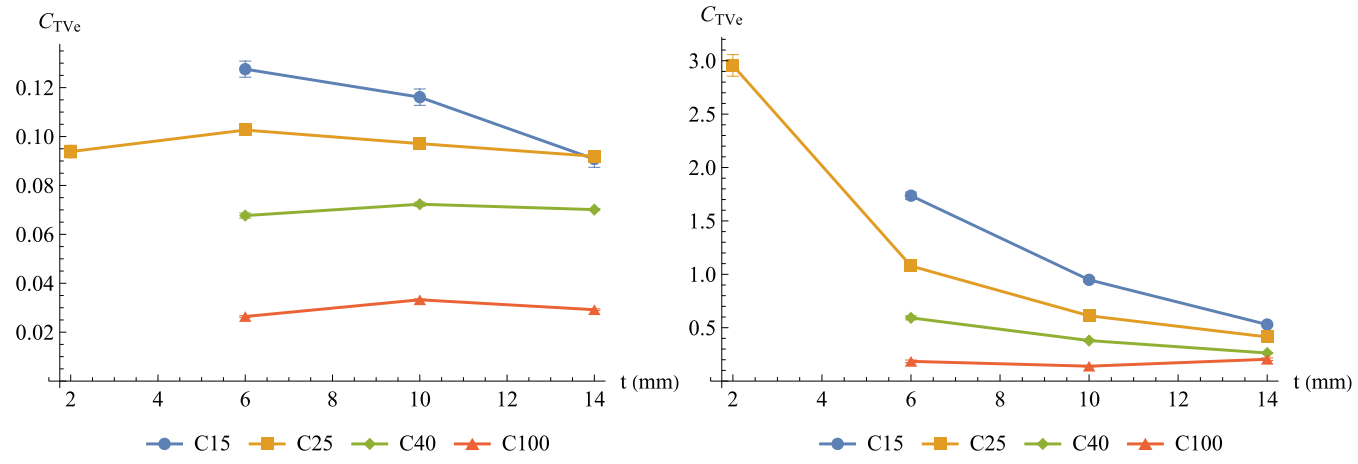

(a) Cell Volume, C_{TVe}

(b) Airfoil Volume, C_{TVe}

Fig. 9. Effective volumetric thrust coefficient behavior based on the cell volume and collector volume.

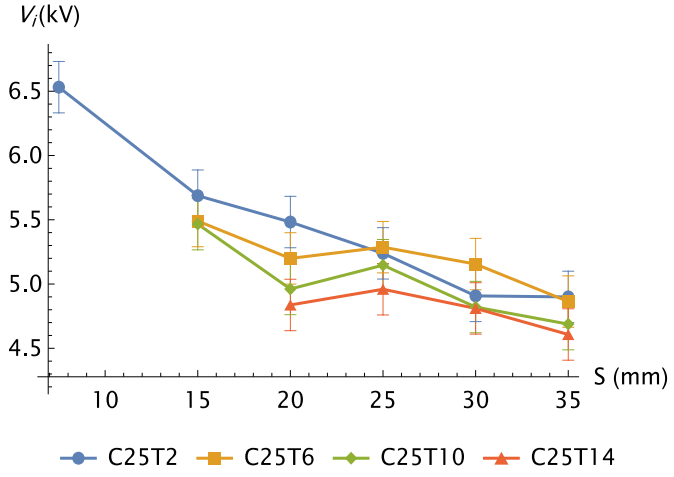

Fig. 10. Ignition voltage vs. spacing.

4.3. Gap and voltage characterization

A variation of the gap d will cause a variation of all the dimensionless parameters introduced in Section 2 since d is chosen as scaling factor for all the lengths; for this reason, a detailed study of the gap influence can assess the capability of the dimensionless parameters to describe the underlying physics. The analysis include voltage variations, since d and V_a contribute to determine the electric field. The C25T6 airfoil, which maximizes C_{Te} for a 20 mm gap, was chosen for this investigation. The measures are performed in the nominal corona regime, before the onset of breakdown which occurs at lower voltages when the gap is reduced. The investigation spans a range of gaps $10 \le d \le 30$ mm and a range of voltages $3 \le V_a \le 20$ kV.

Fig. 14 shows the variation of the dimensional parameters with respect to the gap and the applied voltage for the C25T6S35 single emitter configuration. The ignition voltage, depicted in Fig. 14(a), increases as the gap is increased, with an apparently obvious trend. However it is noteworthy that this phenomenon is related to what is shown in Fig. 10, where a decrease in spacing S results in an increase of the ignition voltage V_i: in fact, according to the scaling introduced in Section 2, the dimensionless spacing is S/d, so an increase in the gap should give similar effects to a reduction of the spacing, i.e. a gap increase with constant inter-emitter spacing and an emitter spacing reduction at constant gap should have similar physical effects. This is indeed confirmed by comparing Figs. 10 and 14(a).

The other dimensional parameters exhibit a behavior consistent with the scaling of Section 2: for instance, the effective thrust is $T_e = C_{Te}\, T_{ref} = C_{Te}\, \epsilon_0 V_a^2/d$, and Fig. 14(b) shows that T_e mainly follows the reference factor V_a^2/d, growing with V_a^2 and decreasing as the gap is increased. Also the power follows its reference factor V_a^3/d^2 and varies inversely with the gap; accordingly, the effective thrust to power ratio exhibits the opposite behavior, scaling as d/V_a. The latter is not easy to determine at low voltages since it is defined as the ratio of two quantities that tend to zero as the applied voltage decreases, and correspondingly the error bars are inherently emphasized.

In general, the trends in Fig. 14 do not indicate that C_{Te}, C_P, C_{TPe} are constant, however their trends are masked by the reference factors, and need a separate analysis.

For the same data of Fig. 14, the behavior of the dimensionless coefficients as a function of *scaled voltage* and gap are presented in Fig. 15. The use of the scaled voltage V_a/V_i automatically includes the influence of the ignition voltage. In this case, the discrete points represent experimental data while the solid lines are modeling functions. For both the effective thrust and power coefficient the following expansion is adopted:

$$f\left(\frac{V_a}{V_i}\right) = c_0 + c_1\left(\frac{V_a}{V_i}\right)^{-1} + c_2\left(\frac{V_a}{V_i}\right)^{-2}. \tag{32}$$

The series is truncated at order 2 in order to avoid over-fitting. The coefficients can depend on d, and a constraint $c_0 + c_1 + c_2 = 0$ is imposed in order to ensure that when the scaled voltage is 1 no thrust is generated ($V_a = V_i$ condition or low voltage limit). Under the opposite condition $V_a \gg V_i$ (high voltage limit) the functions inherently tend to constant values.

The trends of the coefficients C_{Te}, C_P, C_{TPe} can now be analyzed in detail. The effective thrust coefficient, as the gap is decreased, shows an initial increase and then a decrease indicating $d = 20$ mm as a local maximum. On one hand, decreasing the gap increases both t/d and S/d which are beneficial, up to a certain extent, to C_{Te}. On the other hand, the c/d parameter, which represents the weight of the drag coefficient in $C_{Te} = C_T - \frac{1}{2}(c/d)C_D$, also increases. This opposite behavior explains the presence of a local maximum.

The power coefficient dependency on the gap exhibits the same local maximum found in C_{Te} with the difference that the variations around this maximum are smaller, especially at high gaps. The explanation for this trend is, once more, due to opposite behavior of

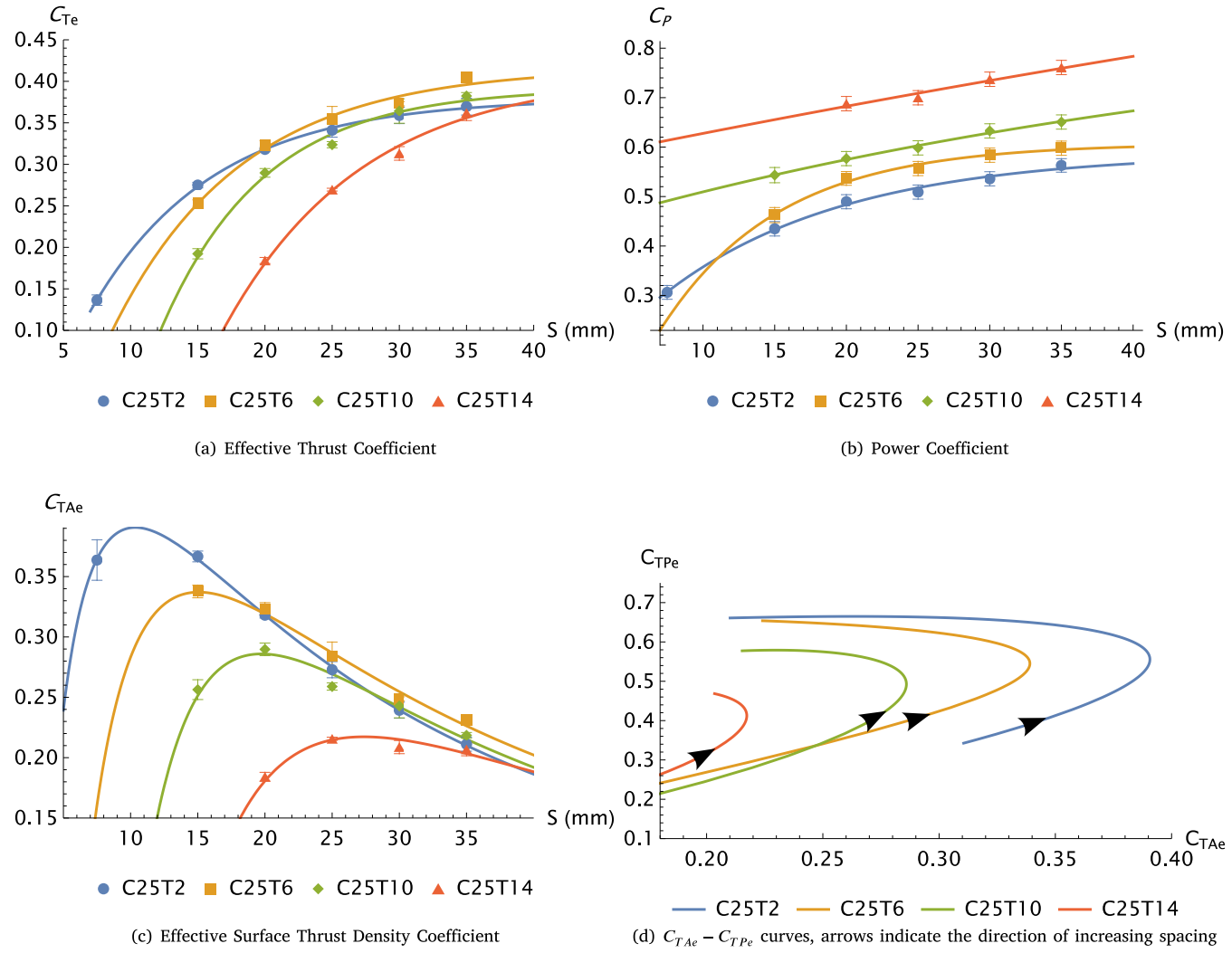

(a) Effective Thrust Coefficient

(b) Power Coefficient

(c) Effective Surface Thrust Density Coefficient

(d) $C_{TAe} - C_{TPe}$ curves, arrows indicate the direction of increasing spacing

Fig. 11. Influence of the inter-collector spacing on the thruster performance for a SE configuration.

the geometrical dimensionless parameters: increasing t/d and S/d increases the power coefficient, whereas increasing c/d reduces it.

The model for the effective thrust to power coefficient C_{TPe} was assumed to be the ratio of the fitting functions for C_{Te} and C_P. In Appendix, using a simple 1D formulation without aerodynamic drag, it is shown that C_{TP} is a constant. As a comparison, in Fig. 15(b) data points tend to a constant trend at high scaled voltages, consistently with Eq. (32). However, at low voltages, the fits ratio becomes less reliable because both the effective thrust and the power coefficient tend to zero. As regards to the dependence on the gap, when d increases C_{TPe} decreases, indicating a trend that is opposite to the dimensional value.

5. Conclusions

This work presents a detailed analysis of the effects of the main geometrical parameters of corona thrusters. In particular, the effects of thickness and chord of airfoil collectors, the spacing between units and the electrodes gap have been studied. The total generated thrust was directly measured by means of load cells, together with the electrical data, including current and ignition and working voltages.

A scaling model was introduced in order to comprehend the relations between experimental data and setup conditions, reducing the number of free parameters. In this model, all the lengths are scaled with respect to the gap, and dimensionless coefficients are defined for all the physical quantities of interest.

It was found that reducing the collector chord is beneficial as the airfoil develops less parasitic drag. However, the thickness value must be carefully chosen to ensure that the resulting shape produces the desired trade-off between good aerodynamics, which requires a small thickness, and suitable electrical performances, which require a large discharge section. Thus, chord to gap and thickness to chord (or thickness to gap) ratios must be controlled together when looking at better performance.

A previous study showed that decreasing the spacing between thruster units results in a loss of thrust due to concurrent blockage effects and electrical shielding; at the same time the thruster size is compacted, so that a local maximum in the thrust density can be found. This is now confirmed, moreover the dependence on spacing in dimensionless form becomes dependence on spacing to gap ratio: in fact, it is found that decreasing the spacing at constant gap has similar effects to increasing the gap at constant spacing.

The scaling model that has been introduced provides an efficient and standardized framework for evaluating results. By using dimensionless numbers, the model reduces the number of free parameters to only four, namely the spacing/gap, chord/gap, thickness/gap ratios and the applied-to-ignition voltage ratio. Other significant parameters like spacing/thickness and thickness/chord can be derived from these four parameters. The impact of each parameter on the dimensionless

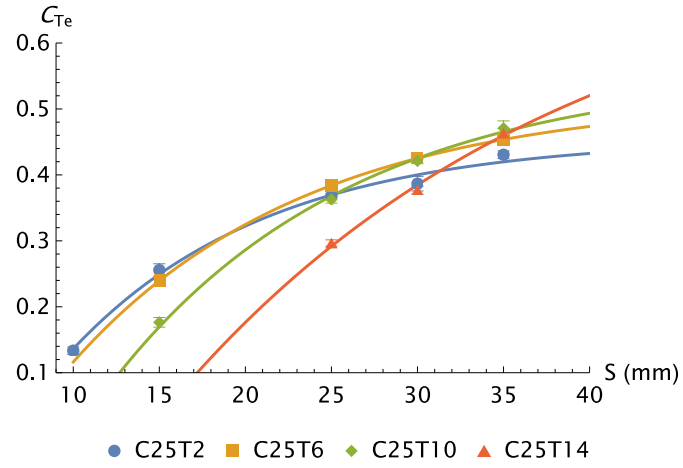

(a) Effective Thrust Coefficient

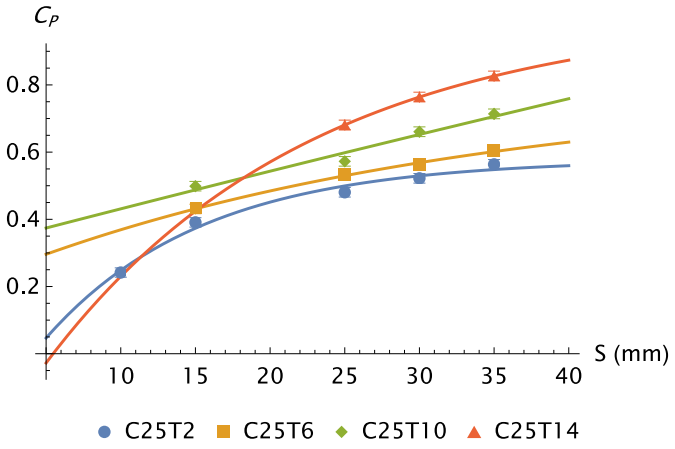

(b) Power Coefficient

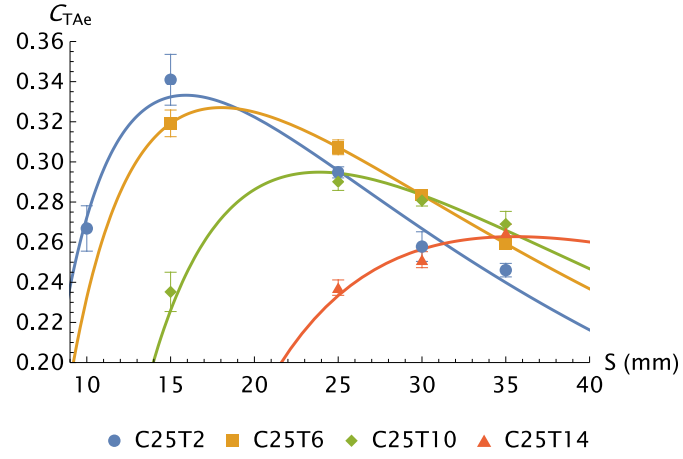

(c) Effective Surface Thrust Density Coefficient

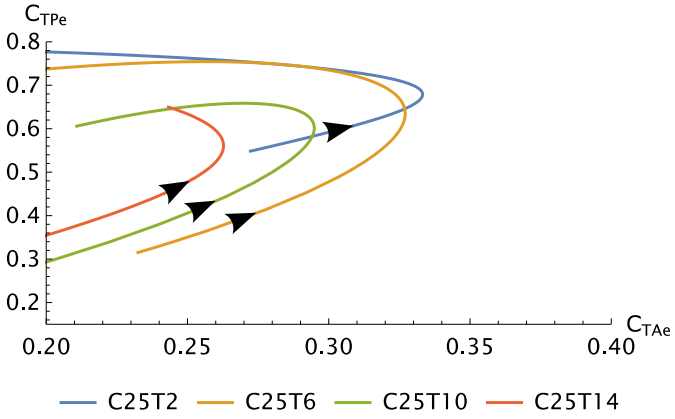

(d) $C_{TAe} - C_{TPe}$ curves, arrows indicate the direction of increasing spacing

Fig. 12. Influence of the inter-collector spacing on the thruster performance for a DE configuration.

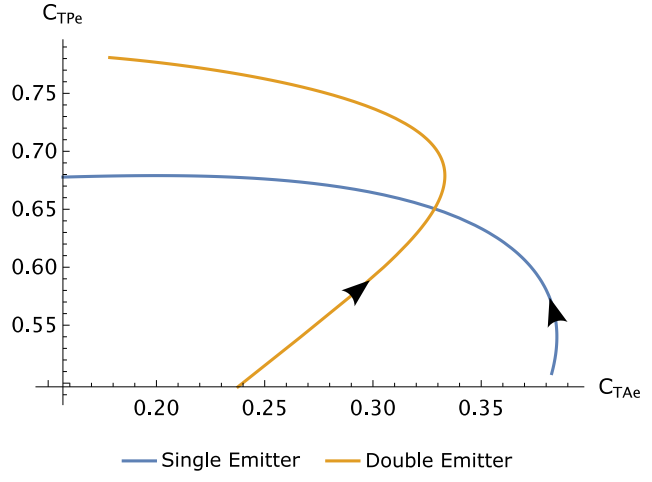

Fig. 13. C25T2 performance in SE and DE configuration; the arrows indicate increasing spacings.

performance indicators has been extensively investigated through the experimental campaign.

A natural development of this work could be identified with a detailed exploration of different electrode geometries coupled with a consistent dimensional analysis of the parameters that govern the ionization process. A further step could also include the effect of a superimposed mean flow, introducing external convection into the scaling model.

Declaration of competing interest

The authors declare that they have no known competing financial interests or personal relationships that could have appeared to influence the work reported in this paper.

Data availability

Data will be made available on request.

Appendix. 1D theory

The scaling model of Section 2 is applied here to a simple 1D geometry, with the aim of solving the scaled equations in this framework and obtain relevant scaling laws for the performance parameters.

The 1D geometry can be imagined as an emitter plane facing a parallel collector plane, separated by a gap d. The x axis spans from the emitters $x = 0$ to the collectors $x = d$, or $0 \leq \hat{x} \leq 1$ in the scaled domain.

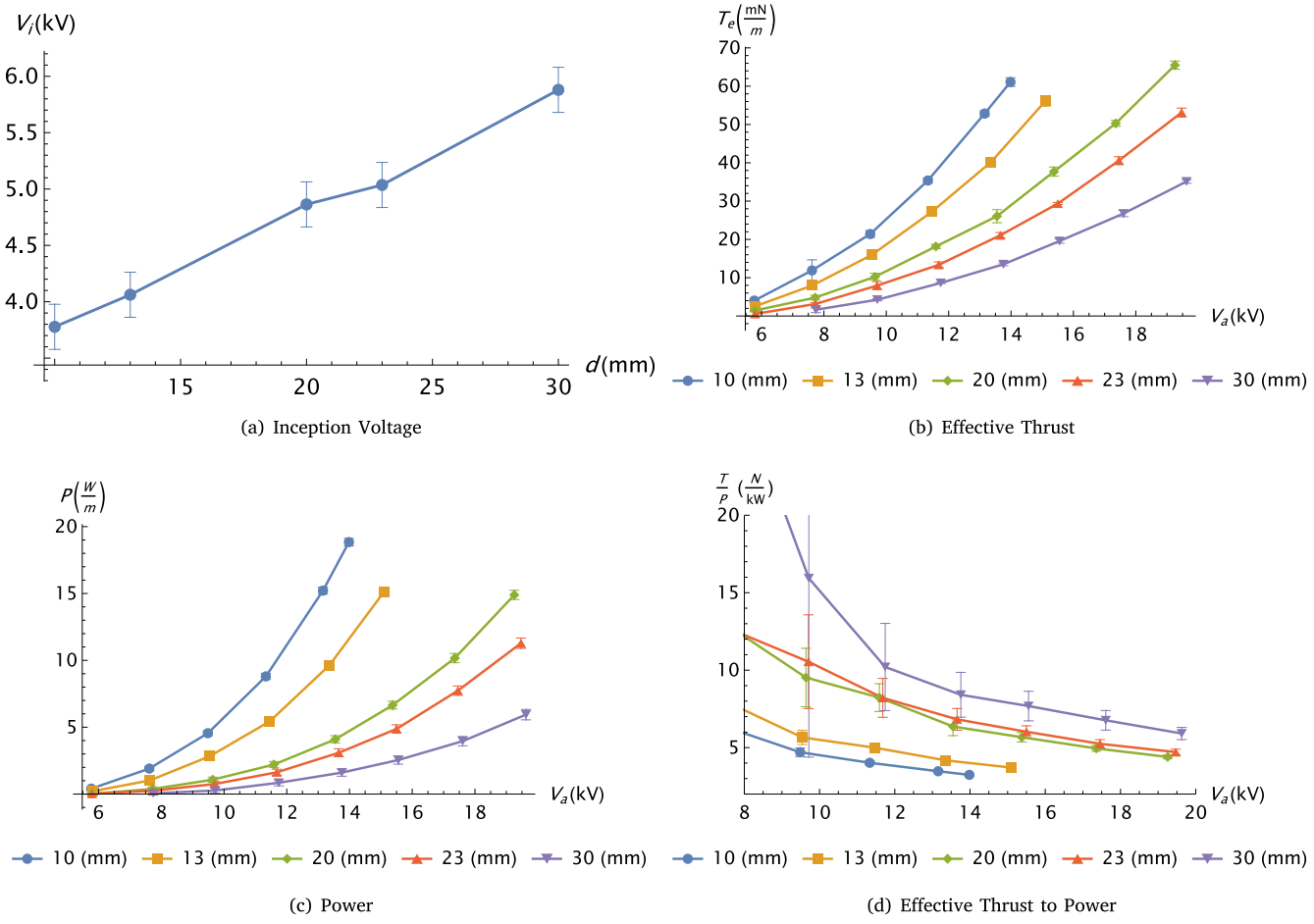

(a) Inception Voltage

(b) Effective Thrust

(c) Power

(d) Effective Thrust to Power

Fig. 14. Influence of the voltage and gap variation on the dimensional performance indicators.

To model such a system, Kapztov's hypothesis [29] is used to describe the ionization region using Peek's boundary condition [28] and setting the dimensionless electric field at the emitter as

$$\hat{E}(0) = \frac{E_i d}{V_a} = \frac{V_i}{V_a} = \hat{V}^{-1}\,, \tag{A.1}$$

where the inception voltage and field are related by $V_i = E_i d$ and $\hat{V}$ is the scaled voltage defined in Eq. (1).

A.1. Solution of the 1D equations

Eqs. (3) for electric field and current are reduced here to the case of the 1D geometry:

$$\begin{cases} \dfrac{\partial \hat{E}}{\partial \hat{x}} = \hat{\rho}_q \\ \dfrac{\partial}{\partial \hat{x}}\ \hat{\rho}_q \hat{E} = 0. \end{cases} \tag{A.2}$$

The second equation can be integrated to yield an integration constant which is the dimensionless current density

$$\hat{\rho}_q \hat{E} = \hat{\jmath}\,, \tag{A.3}$$

and substituting this expression in the first Eq. (A.2) it is obtained

$$\hat{E}\ \frac{\partial \hat{E}}{\partial \hat{x}} = \hat{\jmath}. \tag{A.4}$$

Using the condition $\hat{E}(0) = V_i/V_a = \hat{V}^{-1}$ this equation can be solved leading to

$$\hat{E}(\hat{x}) = \sqrt{2\,\hat{\jmath}\,\hat{x} + \hat{V}^{-2}}. \tag{A.5}$$

This expression for the electric field can be integrated on the scaled domain [0,1]: the left hand term becomes the potential difference across the gap, which in dimensionless form is $V_a/V_a = 1$, and the result is the equation

$$1 = \frac{-\hat{V}^{-3} + (2\hat{\jmath} + \hat{V}^{-2})^{3/2}}{3\hat{\jmath}}\,, \tag{A.6}$$

which admits the following closed form solution for $\hat{\jmath} \geq 0$:

$$\hat{\jmath} = \frac{9 - 12\hat{V}^{-2} + \sqrt{(3 - 2\hat{V}^{-1})^3\ (3 + 6\hat{V}^{-1})}}{16}. \tag{A.7}$$

This function, plotted in Fig. A.16, has distinct asymptotic behaviors in the low and high voltage limits. When the voltage starts rising from the inception voltage, $(\hat{V} - 1)$ is small and the current density trend is nearly linear,

$$\hat{\jmath} = 2\ (\hat{V} - 1) + O[\ (\hat{V} - 1)^2]. \tag{A.8}$$

When the voltage is high, the function has the asymptotic behavior

$$\hat{\jmath} = \frac{9}{8} - \frac{3}{2}\hat{V}^{-2} + O(\hat{V}^{-3})\,, \tag{A.9}$$

so that when $\hat{V} \to \infty$, i.e. under the choked condition $E(0) \to 0$, the Mott-Gurney law $\hat{\jmath} = 9/8$ is correctly recovered [21,32].

A.2. Thrust and electrical power coefficients

In 1D, the integral for the thrust reads

$$C_T = \int_0^1 \hat{\rho}_q \hat{E}\ \mathrm{d}\hat{x} = \hat{\jmath}. \tag{A.10}$$

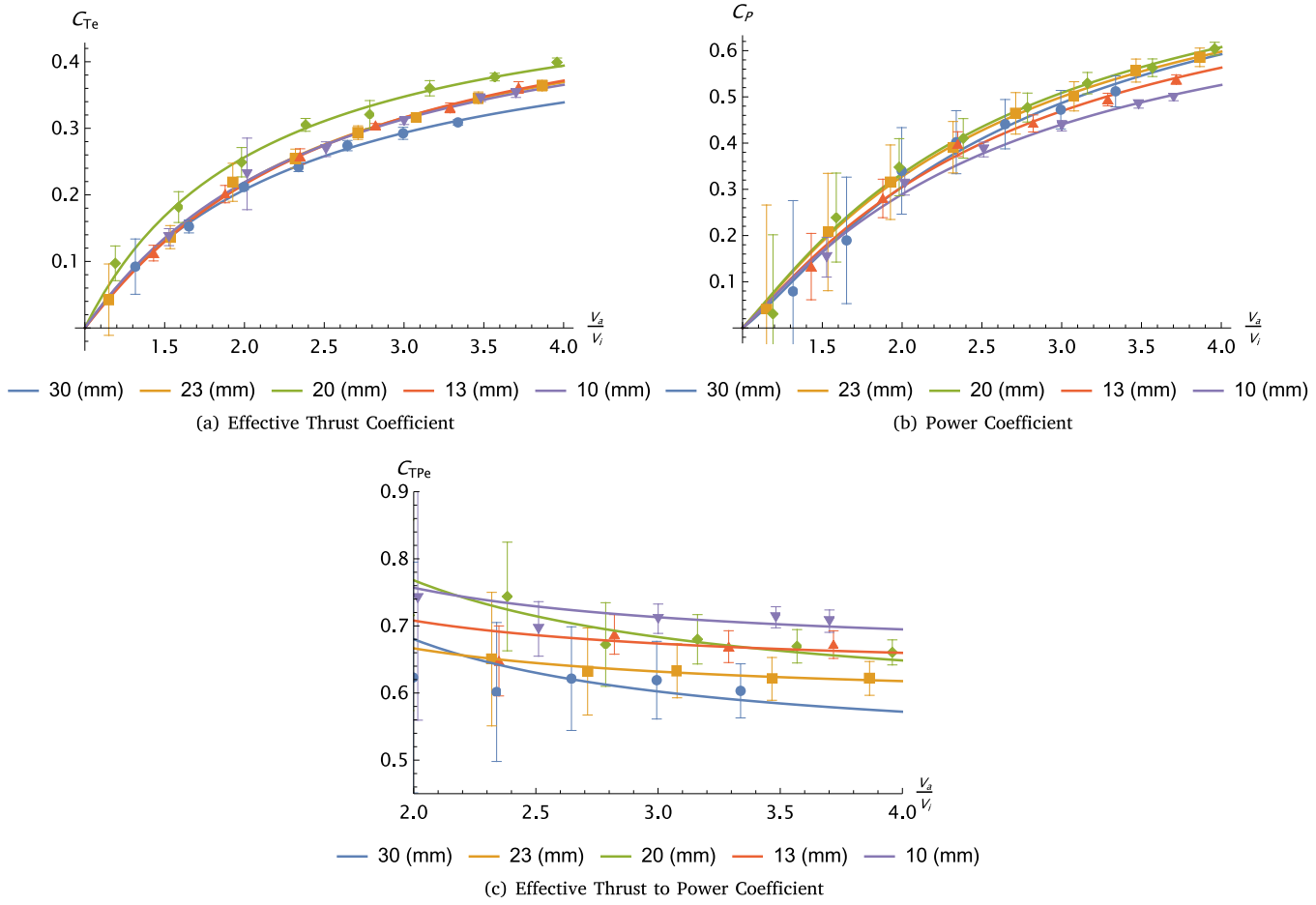

(a) Effective Thrust Coefficient

(b) Power Coefficient

(c) Effective Thrust to Power Coefficient

Fig. 15. Influence of gap and voltage variations on the behavior of the dimensionless coefficients.

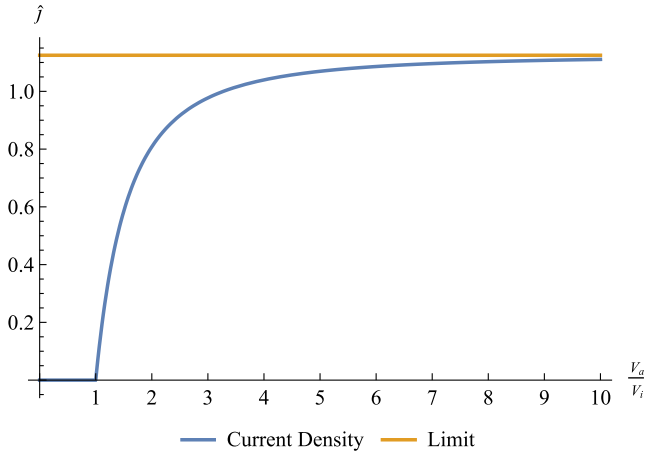

Fig. A.16. Current density curve.

The ideal thrust coefficient without drag is therefore equal to the dimensionless current density, constant on the domain. The electrical power coefficient integral is

$$C_P = \int_0^1 \hat{\jmath}\ \hat{E}\ \mathrm{d}\hat{x} = \hat{\jmath} \int_0^1 \hat{E}\ \mathrm{d}\hat{x} = \hat{\jmath} = C_T. \tag{A.11}$$

Hence, for a 1D configuration

$$C_{TP} = \frac{C_T}{C_P} = 1. \tag{A.12}$$

References

[1] W. Cao, B.C. Mecrow, G.J. Atkinson, J.W. Bennett, D.J. Atkinson, Overview of electric motor technologies used for more electric aircraft (MEA), IEEE Trans. Ind. Electron. (2012).

[2] B.J. Brelje, J.R. Martins, Electric, hybrid, and turboelectric fixed-wing aircraft: A review of concepts, models, and design approaches, Prog. Aerosp. Sci. (2019).

[3] D.M. Goebel, I. Katz, Fundamentals of Electric Propulsion: Ion and Hall Thrusters, John Wiley & Sons, 2008.

[4] S. Mazouffre, Electric propulsion for satellites and spacecraft: Established technologies and novel approaches, Plasma Sources. Sci. Technol. (2016).

[5] C. Charles, Plasmas for spacecraft propulsion, J. Phys. D: Appl. Phys. (2009).

[6] J. Wilson, H. Perkins, W. Thompson, An investigation of ionic wind propulsion, 2009.

[7] E. Moreau, N. Benard, J.-D. Lan-Sun-Luk, J.-P. Chabriat, Electrohydrodynamic force produced by a wire-to-cylinder dc corona discharge in air at atmospheric pressure, J. Phys. D: Appl. Phys. 46 (47) (2013) 475204.

[8] N. Monrolin, F. Plouraboué, O. Praud, Electrohydrodynamic thrust for in-atmosphere propulsion, AIAA J. 55 (2017) 4296–4305.

[9] A. Ieta, M. Chirita, Electrohydrodynamic propeller for in-atmosphere propulsion; rotational device first flight, J. Electrost. (2019).

[10] V. Khomich, V. Malanichev, I. Rebrov, Electrohydrodynamic thruster for near-space applications, Acta Astronaut. 180 (2021) 141–148.

[11] N. Vega, H. Xu, J. Abel, S. Barrett, Performance of decoupled electroaerodynamic thrusters, Appl. Phys. Lett. 118 (2021).

[12] M. Chirita, A. Ieta, First rotary ionic engine with contra-rotating propellers, J. Propuls. Power (2022) 1–8.

[13] H. Xu, Y. He, K. Strobel, C. Gilmore, S. Kelley, C. Hennick, T. Sebastian, M. Woolston, D. Perreault, S. Barrett, Flight of an aeroplane with solid-state propulsion, Nature 563 (2018).

[14] V.Y. Khomich, V.A. Yamshchikov, Electrohydrodynamic flow for the active control of gas flows, Phys.-Usp. (2017).

[15] V. Khomich, I. Rebrov, In-atmosphere electrohydrodynamic propulsion aircraft with wireless supply onboard, J. Electrost. (2018).

[16] L. Zhao, K. Adamiak, EHD gas flow in electrostatic levitation unit, J. Electrost. 64 (7) (2006) 639–645.

[17] A. Martins, M. Pinheiro, Modeling of an EHD Corona flow in nitrogen gas using an asymmetric capacitor for propulsion, J. Electrost. 69 (2) (2011) 133–138.
[18] M. Belan, L. Arosti, R. Polatti, F. Maggi, S. Fiorini, F. Sottovia, A parametric study of electrodes geometries for atmospheric electrohydrodynamic propulsion, J. Electrost. 113 (2021) 103616.
[19] M. Belan, R. Terenzi, S. Trovato, D. Usuelli, Effects of the emitters density on the performance of an atmospheric ionic thruster, J. Electrost. 120 (2022) 103767.
[20] R. Vaddi, Y. Guan, A. Mamishev, I. Novosselov, Analytical model for electrohydrodynamic thrust, Proc. R. Soc. Lond. Ser. A Math. Phys. Eng. Sci. 476 (2020).
[21] K. Masuyama, S. Barrett, On the performance of electrohydrodynamic propulsion, R. Soc. Lond. Proc. Ser. A 469 (2013) 20623.
[22] C. Gilmore, S. Barrett, Electrohydrodynamic thrust density using positive corona-induced ionic winds for in-atmosphere propulsion, Proc. R. Soc. A 471 (2015) 20140912.
[23] A. Ieta, R. Ellis, D. Citro, M. Chirita, J. D'Antonio, Characterization of corona wind in a modular electrode configuration, 2013.
[24] E.M. Calvo, M.J. Pinheiro, P.A. Sá, Modeling of electrohydrodynamic (EHD) plasma thrusters: Optimization of physical and geometrical parameters, Appl. Sci. (2022).
[25] A.A. Ramadhan, N. Kapur, J.L. Summers, H.M. Thompson, Numerical modelling of electrohydrodynamic airflow induced in a wire-to-grid channel, J. Electrost. (2017).
[26] A.X. Moronis, N. Simou, K.N. Kiousis, E.D. Fylladitakis, A model for determining the unipolar ionic saturation current in parallel wire-cylinder electrodes during corona discharge, IEEE Trans. Dielectr. Electr. Insul. (2014).
[27] S. Chen, Y. Zhu, J. Tu, F. Wang, Numerical investigation of an electroaerodynamic driven aeroplane: electrical properties, ionic wind and flight performance, J. Phys. D: Appl. Phys. (2019).
[28] F. Peek, Dielectric Phenomena in High Voltage Engineering, McGraw-Hill Book Company, Incorporated, 1920.
[29] N. Kaptsov, Elektricheskie Yavleniya v Gazakh i Vakuume, 1947.
[30] J. Townsend, XI. The potentials required to maintain currents between coaxial cylinders, Lond. Edinb. Dublin Philos. Mag. J. Sci. 28 (163) (1914) 83–90.
[31] F. Chen, Introduction to Plasma Physics and Controlled Fusion, Springer International Publishing, 2016, pp. 355–411.
[32] N. Mott, R. Gurney, Electronic Processes in Ionic Crystals, in: The International Series of Monographs on Physics, Clarendon Press, 1957.
[33] J. Lemetayer, C. Marion, D. Fabre, F. Plouraboué, Multi-inception patterns of emitter array/collector systems in DC corona discharge, J. Phys. D: Appl. Phys. 55 (2022).